A three-dimensional in-situ self-electrolysis system based on $Ni_3(HITP)_2$/graphene-based composite aerogel particle electrodes for efficient deep removal of phenol from coking wastewater

Shaojun Gao [a], Weifeng Liu [a,*], Meiling Wang [a], Zongbin Zhao [b], Xuguang Liu [a,*]

[a] Institute of New Carbon Materials, College of Materials Science and Engineering, Taiyuan University of Technology, Taiyuan 030024, China
[b] State Key Laboratory of Fine Chemicals, Liaoning Key Laboratory for Energy Materials and Chemical Engineering, School of Chemical Engineering, Dalian University of Technology, Dalian 116024, China

ABSTRACT

Herein, a $Ni_3(HITP)_2$/graphene-based composite aerogel ($Ni_3(HITP)_2$/GA) particle electrode is developed for the oxidation removal of phenol with three-dimensional electrode technology. The as-constructed three-dimensional electrode system possesses high in-situ self-electrolysis capacity and achieves highly efficient degradation of phenol, completely removed within 15 min with a decomposition rate constant of 0.3283 min^{-1}. $Ni_3(HITP)_2$ in $Ni_3(HITP)_2$/GA and the tetradentate $Ni–N_2O_2$ coordination bond generated at the composite interface produce H_2O_2 highly selectively via the 2e- ORR pathway. The graphene layer converts H_2O_2 into •OH by using the 1e- of $Ni_3(HITP)_2$ excitation and the microelectrode action of the particle electrode. Furthermore, the simultaneous generation of •OH and $O_2^{•-}$ in the system greatly reduces the dependence on acidic environment and broadens the scope of utilization. The present work provides a new strategy for the efficient construction of particle electrodes in 3D electrode systems, which allows their potential application in the purification of coking wastewater.

1. Introduction

As the main pollution-like wastewater brought by coal coking process, coking wastewater contains a complex composition of organic pollutants, of which phenolic compounds account for 47%, with phenol accounting for 30% of the total phenols, the largest proportion.[1,2] High concentrations of phenol are strongly corrosive and can cause poisoning, coma, and even death when they enter the body. When phenol wastewater enters the environment, even at very low concentrations, it can be a great threat to the environment and to organisms in water.[3,4] Therefore, the development of a deep treatment process for phenol in coking wastewater is an urgent need for environmental protection.

For deep treatment of phenol, electrochemical oxidation has been widely used for its simplicity, high reaction rate, and low secondary pollution effects.[5] In particular, there has been interest in emerging three-dimensional (3D) electrode technologies, which is a new electrochemical reaction system formed by filling or suspending some particulate materials between the two-dimensional (2D) electrodes in traditional two-dimensional electrochemical system.[6] During

electrochemical reaction, these particle electrodes are easily polarized under the electrostatic induction of applied electric field, forming a large number of charged microelectrodes on which electrochemical redox reactions take place.[7] 3D electrode technology has the merits of larger specific surface area, stronger mass transfer capacity, and higher current efficiency than conventional 2D electrode system,[8,9] as a result, it consumes less energy and is more efficient in pollutant degradation.

The preparation of efficient and stable particle electrodes in three-dimensional electrode systems is the prerequisite. Particle electrode materials have undergone development from single phase to multiphase, and their corresponding performance in treating wastewater is becoming stronger.[10] Currently, carbon-based composites have attracted a large amount of attention from researchers owing to their high porosity, large specific surface area, multidimensional charge transfer pathways, and excellent electrical conductivity. Shi et al.[11] developed a nitrogen-doped mesoporous carbon particle electrode with good phenol removal over a wide pH range, which was modified with $NiO/CeO_2/MnO_2$ to improve the degradation performance in an acidic environment. Ghanbarlou et al.[12] synthesized a nitrogen-doped iron/graphene-based particle electrode catalyst by a one-step

---

high-temperature annealing method with Prussian blue as the precursor, in which the introduction of iron triggered the Fenton reaction to produce hydroxyl radical(●OH) for enhanced degradation of Bisphenol A. However, the catalytic efficiency of this system is only about 30% higher than that of the two-dimensional electrode system. In this system, it is ●OH that effectively but non-selectively oxidizes organic pollutants and thus achieves their degradation. At present, most of such systems use Fenton or Fenton-like reactions between the transition metal loaded on the particle electrode and the H_2O_2 generated from the reduction of dissolved oxygen at the cathode to enhance the performance degradation of organic pollutants.[13,14] The particle electrode material itself has fewer catalytic active sites, resulting in poor electrocatalytic oxygen reduction performance and almost no H_2O_2 production. Their practical applications are limited by their high energy consumption and reliance on the main electrode.

Conductive metal-organic frameworks (c-MOF) have the advantages of high electrical conductivity and abundant catalytic active sites, as well as the large specific surface area and microporous structure of MOF, which endow them with great potential for application as electrocatalytic oxygen reduction materials.[15,16] Elise M et al. [17] used high conductivity $Ni_3(HITP)_2$ (HITP: Hexaiminotriphenylene) as an electrocatalytic oxygen reduction material, showing superior ability to produce H_2O_2 comparable to the most active non-platinum group metal electrocatalysts in terms of oxygen reduction activity and stability. In various catalytic reactions, electrons transfer from the active metal core to the carbon layer, then they excite the electrocatalytic activity on the carbon surface.[18] Therefore, graphite-shell c-MOF hybrid carbon electrode is considered as a promising particle electrode material. The encapsulated c-MOF exerts its excellent oxygen reduction performance to in-situ generate a large amount of H_2O_2 in the material itself through the $2e^-$ path, and the electrocatalytic activity of the outer graphitic shell is activated to provide $1e^-$ to convert H_2O_2 into ●OH in situ. Therefore, the three-dimensional electrode system combined with graphite-shell c-MOF hybridized carbon particle electrode is expected to construct a 3D in-situ self-electrolytic system(3D-ISES).

In the present work, a $Ni_3(HITP)_2$/graphene-based composite aerogel particle electrode with high electrical conductivity and high catalytic activity was developed by using graphene carbon aerogel as the substrate and $Ni_3(HITP)_2$ with high electrocatalytic activity as the composite unit. Combined with the three-dimensional electrode technology, a three-dimensional in situ self-electrolysis system was constructed, in which the components in the system give full play to their respective roles and synergistically produce the optimal degradation effect. In this system, $Ni_3(HITP)_2$ and the tetradentate $Ni–N_2O_2$ coordination bonds at the composite interface catalyze the generation of H_2O_2 through a $2e^-$ pathway with high selectivity, and the graphene layer converts H_2O_2 into ●OH by using $Ni_3(HITP)_2$ to stimulate $1e^-$ transfer and the microelectrode effect of particle electrode, so as to achieve the effect of highly efficient and deep degradation of phenol in coking wastewater. The electrolytic system proposed in this study can significantly improve the degradation efficiency of the three-dimensional electrode system and reduce energy consumption. Meanwhile, the conformational relationship between the unique structure of the composite aerogel and the high ●OH generation capacity was investigated. The intrinsic mechanism of the reaction species and efficient degradation activity involved in the system was elucidated.

2. Experimental section

2.1. Preparation of $Ni_3(HITP)_2$/graphene-based composite aerogel

The graphene oxide dispersion (2 mg mL^{-1}, 3 mL) was mixed with different mass ratios of $Ni_3(HITP)_2$(0.3, 0.5, 0.7, and 0.9, separately), stirred and sonicated well. Then ammonia (100 μL) was added to it and sonicated well. The vial containing the mixed solution was placed in a reactor and reacted at 150 °C for 12 h, thus obtaining $Ni_3(HITP)_2$/

graphene-based composite hydrogel. The obtained hydrogel was washed and soaked in 15% ethanol aqueous solution for 48 h, and finally freeze-dried to obtain $Ni_3(HITP)_2$/graphene-based composite aerogel ($Ni_3(HITP)_2$/GA). The same preparation process, without $Ni_3(HITP)_2$ being added, was adopted to prepare graphene aerogel (GA).

2.2. Three-dimensional electrode performance test for phenol degradation

The volume of the 3D electrode reactor was 180 mL, and the anode and cathode were stainless steel electrodes (80 mm × 45 mm×1 mm) with 7 cm spacing between two electrode plates. The whole electrolytic tank was placed on a magnetic stirrer to mix the solution evenly and improve the mass transfer capacity by stirring. A sieve plate inside the tank separated the rotor from the particle electrodes to prevent the particle electrodes from being mechanically stirred up. Phenol solution (150 mL) was added to the reactor and sampling was performed at predetermined time intervals. Na_2SO_4 (0.05 M) was used as the electrolyte. $Ni_3(HITP)_2$/GA was soaked in phenol solution for 0.5 h before the experiment to reduce the adsorption effect. To keep experiment accuraly, each set of experiments was repeated three times. In addition, oxygen was continuously flowed during the experiment to ensure enough dissolved oxygen. In this study, the phenol degradation process in most cases can be well described by a pseudo-first-order model with Eq. (1):

$$\ln(C_0/C_t) = kt \tag{1}$$

where t is reaction time (min), k (min^{-1}) degradation rate constant, and C_0 and C_t the concentrations of phenol at beginning and at time t, respectively. $\ln(C_0/C_t)$ is linearly related to t, and k is determined as the slope of the linear plot.

The concentration of phenol in the samples was determined by using a UV spectrophotometer (HACH, DR6000). H_2O_2 content was determined spectrophotometrically with iodine reagent. COD assay was performed by potassium dichromate method.

3. Results and discussion

3.1. Preparation and characterization of $Ni_3(HITP)_2$/GA

The schematic diagram of the overall preparation process of $Ni_3(HITP)_2$/graphene composite aerogel ($Ni_3(HITP)_2$/GA) is shown in Fig. 1. First, ammonia is added to aqueous graphene oxide solution. Then, positively charged $Ni_3(HITP)_2$ was introduced under stirring and sonication, followed by hydrothermal treatment at 150 °C for 12 h, during which $Ni_3(HITP)_2$ and graphene oxide were mixed and assembled continuously under electrostatic effect, while graphene oxide was assembled into hydrogel by reduction. Finally, $Ni_3(HITP)_2$/graphene composite aerogel ($Ni_3(HITP)_2$/GA) was prepared by lyophilization. During the assembly process, various interactions occur between graphene oxide lamellae and $Ni_3(HITP)_2$: (1) electrostatic interactions between the negatively charged graphene oxide and the positively charged $Ni_3(HITP)_2$; (2) the graphene oxide is rich in carboxyl groups, which are easily ionized to carboxylate. The carboxylic acid radicals ligated with the abundant Ni^{2+} in the $Ni_3(HITP)_2$ structure, thus forming a tetradentate $Ni–N_2O_2$ coordination bond; (3) both graphene oxide and $Ni_3(HITP)_2$ structures have abundant benzene ring structures, which form a strong π-π stacking interaction. Under the action of multiple mutual forces, graphene oxide and $Ni_3(HITP)_2$ support each other and assemble into a three-dimensional structure with a porous structure.

Table S1 shows the zeta potentials of GO, $Ni_3(HITP)_2$, $0.3Ni_3(HITP)_2$/GA, $0.5Ni_3(HITP)_2$/GA, $0.7Ni_3(HITP)_2$/GA, and $0.9Ni_3(HITP)_2$/GA. The zeta potential of GO was − 49.7 mV at pH= 7, indicating that the system consists of uniformly dispersed and highly stable negatively charged particles [19]. Alternatively, $Ni_3(HITP)_2$ aqueous solution possesses a zeta potential of + 13.22 mV.

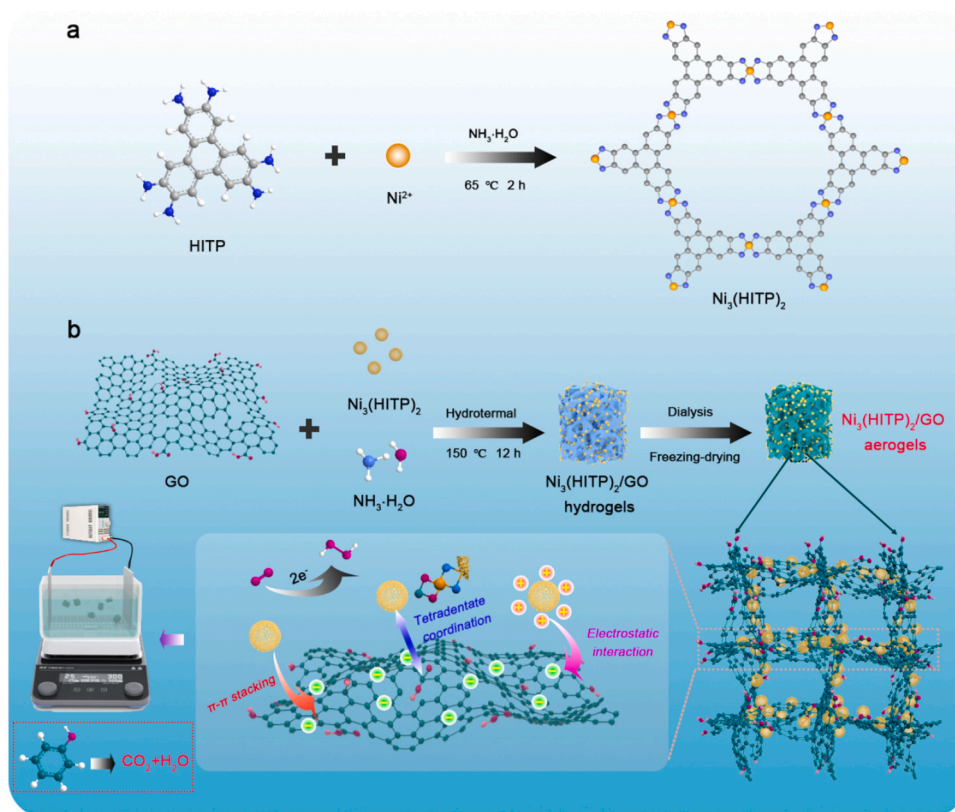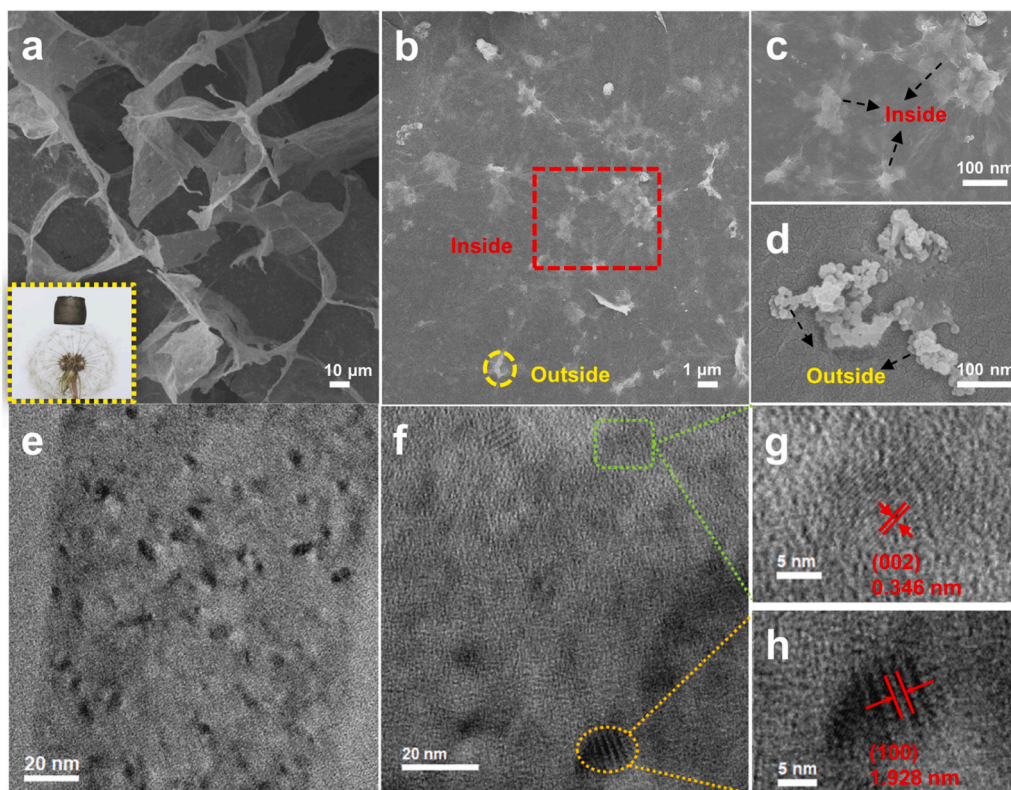**Fig. 1.** Schematic diagram of the preparation process of $Ni_3(HITP)_2$/GA.

Fig. 2. (a–d) SEM images of $0.7Ni_3(HITP)_2$/GA under different magnifications; (e–h) TEM image of $0.7Ni_3(HITP)_2$/GA.

0.3Ni₃(HITP)₂/GA, 0.5Ni₃(HITP)₂/GA, 0.7Ni₃(HITP)₂/GA, and 0.9Ni₃(HITP)₂/GA display decreasing zeta potential values with increasing Ni₃(HITP)₂. The decrease of the absolute value of zeta potential indicates that the system becomes more and more unstable owing to the lack of electrostatic repulsion [20]. Therefore, the addition of excessive Ni₃(HITP)₂ leads to the agglomeration of the dispersions. As shown in Fig. S1(b) and (c) for the recovery states of 0.7Ni₃(HITP)₂/GA and 0.9Ni₃(HITP)₂/GA after compression with 100 g weights, respectively, 0.9Ni₃(HITP)₂/GA is destroyed in the whole aerogel state after compression. In addition, Fig. S2(a–c) further illustrates that among the Ni₃(HITP)₂/GA samples synthesized with different doping ratios and reaction temperatures and times, and hydrothermally treated at 150 °C for 12 h, 0.7Ni₃(HITP)₂/GA exhibits the best 3D electrocatalytic degradation of phenol. FESEM was used to investigate the morphology of Ni₃(HITP)₂/GA after Ni₃(HITP)₂ addition (Fig. S3). When the mass ratio of Ni₃(HITP)₂ to GO is 0.7, the structure of the obtained product is optimal, and Ni₃(HITP)₂ is uniformly distributed, while the pore structure is abundant. In conjunction with Fig. 2(a–d), these results suggest that 0.7Ni₃(HITP)₂/GA with rich network structures may increase mass transfer channels and shorten mass transfer distances [21]. Moreover, Ni₃(HITP)₂ particles in between graphene oxide lamellae improve the mechanical properties of Ni₃(HITP)₂/GA, as well as increasing active site exposure, which is beneficial to improving degradation efficiency [22]. At the same time, Ni₃(HITP)₂ particles are loaded on the graphene sheet layer or are encapsulated. Where the graphene sheet layer encapsulates Ni₃(HITP)₂ particles under the attractive effect of Ni₃(HITP)₂ on it, the sheet layer keeps approaching Ni₃(HITP)₂ and finally forms an encapsulated shape. The loading of Ni₃(HITP)₂ promotes oxygen adsorption and conversion to H₂O₂ [23,24]. On the other hand, the encapsulated Ni₃(HITP)₂ stimulates the electrocatalytic activity of the graphene shell layer, which provides electrons for the generation of •OH [18,25–27]. The HRTEM observation (Fig. 2(e–h)) shows that Ni₃(HITP)₂ particles are uniformly distributed across graphene sheets, and the further magnification of the Ni₃(HITP)₂ nanoparticles indicates that their lattice stripes have a spacing of 1.928 nm, which corresponds

to the crystal plane (100) of Ni₃(HITP)₂ [28]. The 0.346 nm stacking distance observed in 0.7Ni₃(HITP)₂/GA composite matches the graphite (002) crystal plane *d*-spacing [29]. In summary, the optimal sample 0.7Ni₃(HITP)₂/GA was obtained by hydrothermal treatment at 150 °C for 12 h. Thereafter, 0.7Ni₃(HITP)₂/GA samples are chosen for subsequent investigations and abbreviated as Ni₃(HITP)₂/GA.

To determine the composition of Ni₃(HITP)₂/GA, powder X-ray diffraction (XRD) was utilized. The diffractograms of Ni₃(HITP)₂/GA are compared with those of GA and Ni₃(HITP)₂ powders (Fig. 3(a)). The diffraction peaks at 2θ ≈ 4.76°, 9.57°, and 26.53° correspond to the (100), (200), and (001) crystal planes of Ni₃(HITP)₂, respectively [27]. The typical peak at 2θ ≈ 24.69° corresponds to the (002) crystal plane formed by the π-π stacking between graphene lamellae in GA [30]. It is worth noting that the graphite characteristic peak in Ni₃(HITP)₂/GA (2θ≈24.69°) shows a clear sign of leftward shift with respect to GA (2θ≈24.96°), which may be due to the reduction of crystal plane spacing and change of crystal structure caused by the introduction of Ni₃(HITP)₂ and special interfacial functional groups. And the occurance of this change also promotes the construction of the three-dimensional structure [31]. In addition, the diffraction peak becomes relatively flat, indicating that the obtained Ni₃(HITP)₂/GA is mainly based on turbostratic carbon [32].

As can be seen from the FTIR spectra (Fig. S4), Ni₃(HITP)₂/GA is rich in active functional groups, with 3437 cm⁻¹ for –OH, 1737 cm⁻¹ for C=O, and 1205 cm⁻¹ for C–N with enhanced stretching vibrational bonds. It is reported that the rich oxygen-containing functional groups in Ni₃(HITP)₂/GA are beneficial to improving the selectivity towards O₂ in the electrocatalytic reduction process [18]. The Raman spectra of all samples (Fig. 3(b)) show two significant D and G bands at 1348 cm⁻¹ and 1580 cm⁻¹, which indicate the defects in the graphite lattice and the in-plane stretching vibrations of ordered carbon sp² hybridization, respectively. Therefore, the I_D/I_G ratio can reflect the degree of graphitization as well as the degree of defects in the material. As shown in Fig. 3(b), the I_D/I_G of Ni₃(HITP)₂/GA is increased to a certain extent compared with GA. The insertion of Ni₃(HITP)₂ nanoparticles into GO
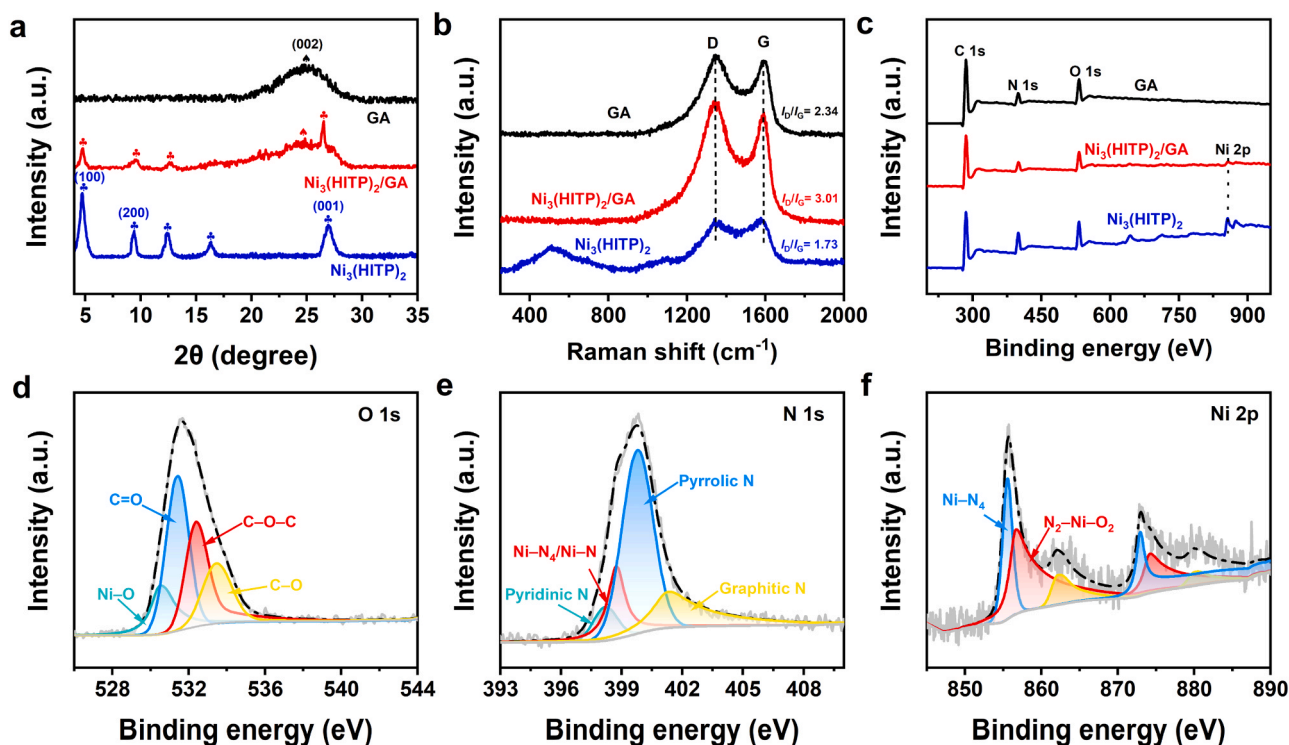

Fig. 3. (a) XRD patterns, (b) Raman spectra, and (c) X-ray photoelectron spectra of GA, Ni₃(HITP)₂, and Ni₃(HITP)₂/GA; (d) O 1 s, (e)N 1 s, and (f) Ni 2p spectra of Ni₃(HITP)₂/GA.

lamellae, thus affecting their stacking degree, leads to an increase in the defect degree of graphite, which is beneficial to the adsorption of O_2 in the subsequent electrocatalytic reduction process [33]. The results also verify the change of crystal structure, as can be concluded from the XRD results.

To further investigate the interaction between $Ni_3(HITP)_2$ and GA in $Ni_3(HITP)_2/GA$, X-ray photoelectron spectroscopy (XPS) analysis was performed (Fig. 3(c–f), S5). In Fig. 3(c), the presence of C, N, O, and Ni elements in $Ni_3(HITP)_2/GA$ indicates the formation of composites. High-resolution N 1 s mapping of $Ni_3(HITP)_2/GA$ (Fig. 3(d)) shows the appearance of a characteristic peak attributed to Ni–N_x at 398.73 eV with respect to GA (Fig. S5), while the high-resolution O 1 s mapping (Fig. 3(e)) shows a Ni–O peak (530.48 eV). Meanwhile, the high-resolution N 1 s mapping of $Ni_3(HITP)_2/GA$ also indicates that the N element in the material is mainly in the form of pyrrolic N, and the presence of large amounts of pyrrolic N significantly enhances the production of H_2O_2 during $2e^-$ ORR [34,35]. Meanwhile, the high-resolution Ni 2p mapping of $Ni_3(HITP)_2/GA$ (Fig. 3(f)) can be deconvoluted into two peaks at 855.61 and 856.83 eV, indicating the existence of two different coordination environments for Ni(II) [36]. The peak at 855.61 eV originates from the abundant Ni–N_4 valence bond in $Ni_3(HITP)_2$, while that at 856.83 eV comes from the Ni(II) at the interface of GO sheet and $Ni_3(HITP)_2$. The latter Ni(II) belongs to Ni–N_2O_2 tetradentate coordination bond, a chemotactic bond that can reduce O_2 to H_2O_2 with high selectivity with respect to the original Ni–N_4 bond in $Ni_3(HITP)_2$ [37]. These results strongly suggest that the Ni(II) in $Ni_3(HITP)_2$ nanoparticles acts as a bridge connecting GO sheet layer and $Ni_3(HITP)_2$, forming a complete $Ni_3(HITP)_2/GA$ 3D structure. In addition, the Ni 2p peak in $Ni_3(HITP)_2/GA$ is reduced by about 0.1 eV compared with $Ni_3(HITP)_2$, but still in the range of Ni^{2+} (Fig. 3(f)), which indicates that some electrons are transferred to $Ni_3(HITP)_2$ owing to the electrostatic interaction between the materials, and the increase in the charge density of Ni (II) site makes it an effective electron donor in the process of electrocatalytic oxygen reduction reaction [38], thus improving the degradation efficiency of three-dimensional electrode.

To investigate the effect of the introduction of $Ni_3(HITP)_2$ on the internal pore structure of $Ni_3(HITP)_2/GA$, the specific surface area as well as the pore structure of the materials were evaluated by nitrogen adsorption-desorption (Fig. 4(a)). The specific surface area of $Ni_3(HITP)_2/GA$ was 236.64 m^2 g^{-1}, higher than that of pure GA (44.18 m^2 g^{-1}), which was brought about by the introduction of $Ni_3(HITP)_2$ with an abundant microporous structure, as also proved by the significant increase of $Ni_3(HITP)_2/GA$ microporous surface area. Meanwhile, the composite aerogel has a hierarchical pore structure with micro-, meso-, and macropores coexisting. The presence of $Ni_3(HITP)_2$ can effectively inhibit the accumulation of graphene flakes and improve their pore structure [39]. The rich pore structure can provide and expose a large number of active sites, and consequently promote the $2e^-$ reduction of O_2 in electrocatalytic reduction process, thus improving the selectivity towards H_2O_2 generation [40]. In addition, the porous structure facilitates the enrichment of pollutants as well as the transfer of electrons, which is conducive to improving the degradation efficiency of phenol. The mechanical properties of the prepared graphene-based aerogel samples were also tested. Both GA and $Ni_3(HITP)_2/GA$ are compressed to more than 90% deformation without collapse when direct compression is performed with a 100 g weight, 10,000 times or more of their self-weight (Fig. S6). When the external force is removed, both structures keep undamaged and fully resume their original heights without exhibiting observable irreversible deformation. By comparing the stress-strain curves (Fig. 4(b)), it can be seen that the maximum stress of $Ni_3(HITP)_2/GA$ (121.51 kPa) is significantly higher than that of GA (16.08 kPa), and the compressive strength of $Ni_3(HITP)_2/GA$ is increased by more than 7.5 times compared with that of pure GA. Meanwhile, $Ni_3(HITP)_2/GA$ can be reversibly deformed at different
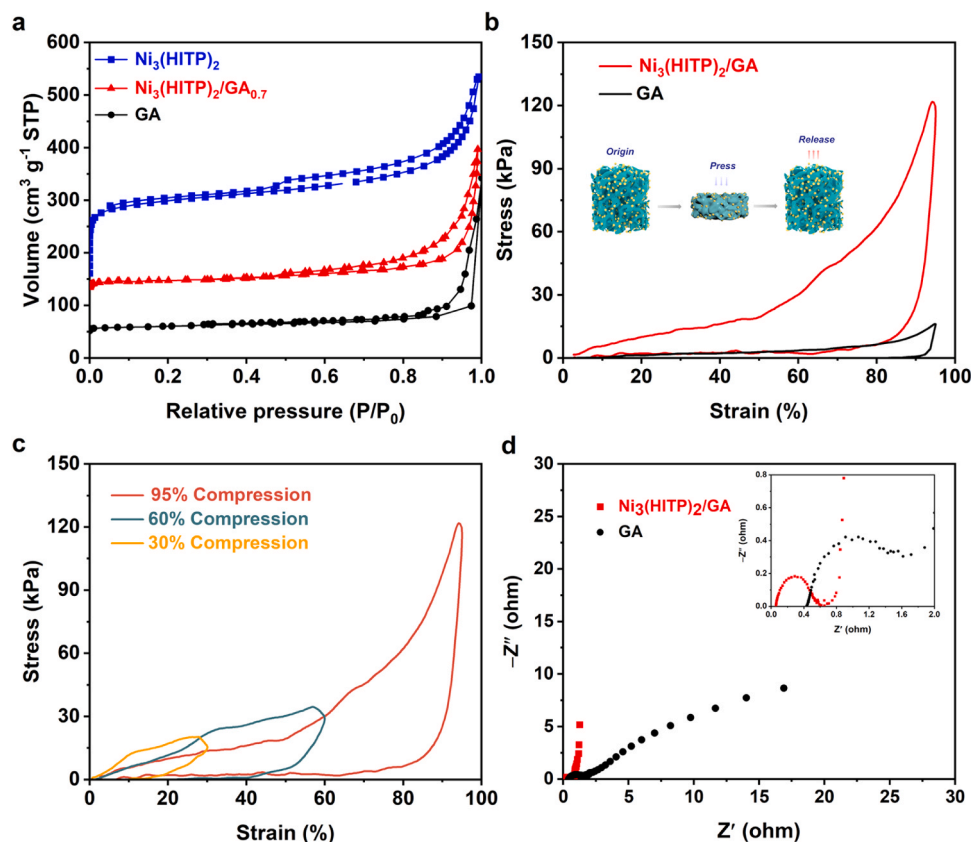

Fig. 4. (a) Nitrogen adsorption–desorption isotherms of $Ni_3(HITP)_2$, GA, and $Ni_3(HITP)_2/GA$; (b) Stress-strain curves of GA and $Ni_3(HITP)_2/GA$ at 95% of the maximum strain; (c) Stress-strain curves of $Ni_3(HITP)_2/GA$ at 30%, 60%, and 95% of the maximum strain; and (d) Nyquist plots of GA and $Ni_3(HITP)_2/GA$.

strains (Fig. 4(c)), i.e., 30%, 60%, and 95%, and exhibits excellent resilience up to a maximum stress of 121.51 kPa. After 10 compression cycles (Fig. S7) at 95% strain, $Ni_3(HITP)_2$/GA remains its height basically the same as the initial value, indicating its reproducibility and reversibility.

In order to evaluate the electrochemical performance of $Ni_3(HITP)_2$/GA composite, cyclic voltammetry, constant current charge/discharge (Fig. S8), and AC impedance (Fig. 4(d)) tests were performed. The cyclic voltammetry (CV) curves of $Ni_3(HITP)_2$/GA composites at different scan rates are shown in Fig. S8(a). The CV curves are basically quasi-rectangular in shape, indicating that the specific capacity of the material is mainly generated by the bilayer with excellent charge transport properties [41]. The comparative CV cycling curves of GA and $Ni_3(HITP)_2$/GA composites obtained at the same scan rate of 20 mV s^{-1} are shown in Fig. S8(b). The area of the CV curve of GA is significantly smaller than that of $Ni_3(HITP)_2$/GA composites, indicating the higher specific capacitance of $Ni_3(HITP)_2$/GA composites than GA. The addition of $Ni_3(HITP)_2$ increases the capacitance of GA under the synergistic effect of the materials. Fig. S8(c) shows the constant current charge/discharge plots of GA and $Ni_3(HITP)_2$/GA at a current density of 0.8 A g^{-1}. The charge/discharge time of GA material is significantly shorter than that of $Ni_3(HITP)_2$/GA composite, indicating that $Ni_3(HITP)_2$/GA composite has a larger capacity, which is consistent with the above CV curve results. The AC impedance (EIS) pattern (Fig. 4(d)) shows that the intermolecular and molecule-collector impedance of $Ni_3(HITP)_2$/GA electrode material is smaller than that of GA, i.e., the resistance to charge transfer is smaller and the electron transfer is faster. The ions in $Ni_3(HITP)_2$/GA composites are subjected to less diffusion resistance during transport process, so their diffusion rate is higher and their electrical conductivity is better. The introduction of $Ni_3(HITP)_2$ improves the electron transfer of GA under a synergistic effect, thus facilitating the electron transfer in the subsequent electrocatalytic reduction process to improve the degradation efficiency [42,43]. The cycling stability performance plots of GA and $Ni_3(HITP)_2$/GA (Fig. S8

(d)) also indicate that $Ni_3(HITP)_2$/GA composites possess excellent cycling stability, which is beneficial to the recycling of the particle electrodes.

3.2. Construction of 3D in-situ self-electrolytic system

Given the excellent properties of $Ni_3(HITP)_2$/GA, it was used as particle electrode to construct a 3D in-situ self-electrolytic system. To clarify the roles of the different electrodes in the system, the electrocatalytic degradation of phenol was conducted under different electrocatalytic systems. The 3D electrolysis device is shown in Fig. S9. As shown in Fig. 5(a), 3D-$Ni_3(HITP)_2$/GA achieves an astounding phenol removal of 100.0% in 15 min. However, for the 2D system, the phenol removal rate is only 23.1% after 15 min treatment. In contrast, the removal rates of phenol by 3D-ACs, $Ni_3(HITP)_2$, and GA are 28.3%, 40.4% and 46.2%, respectively. The decomposition rate constants (k_{obs}) for different systems were obtained according to the pseudo-first-order kinetic equation (Fig. 5(b)). There is a higher decomposition rate constant for phenol in all three-dimensional systems than in two-dimensional systems (0.0154 min^{-1}). Also, there is a much higher decomposition rate constant for phenol over 3D-$Ni_3(HITP)_2$/GA (0.3283 min^{-1}) than over 3D-ACs (0.0204 min^{-1}), 3D-$Ni_3(HITP)_2$ (0.0371 min^{-1}), and 3D-GA (0.0479 min^{-1}) systems, with a value 6.85 times that of 3D-GA system. To further demonstrate the reason for this striking effect, the in-situ hydrogen peroxide production was measured. The results show (Fig. 5(c)) that when $Ni_3(HITP)_2$ alone is used as a particle electrode, it produces the highest amount of hydrogen peroxide. This is mainly due to its special ligand structure that generates a large amount of H_2O_2 from O_2 along a 2e$^-$ pathway [44,45]. In contrast, the 3D-$Ni_3(HITP)_2$/GA system produces essentially no hydrogen peroxide, mainly because the system promptly converts H_2O_2 into ●OH through the special interface between $Ni_3(HITP)_2$ and GA.

Moreover, in order to demonstrate the advantages of the 3D electrode, the degradation efficiency of the particulate electrode material in
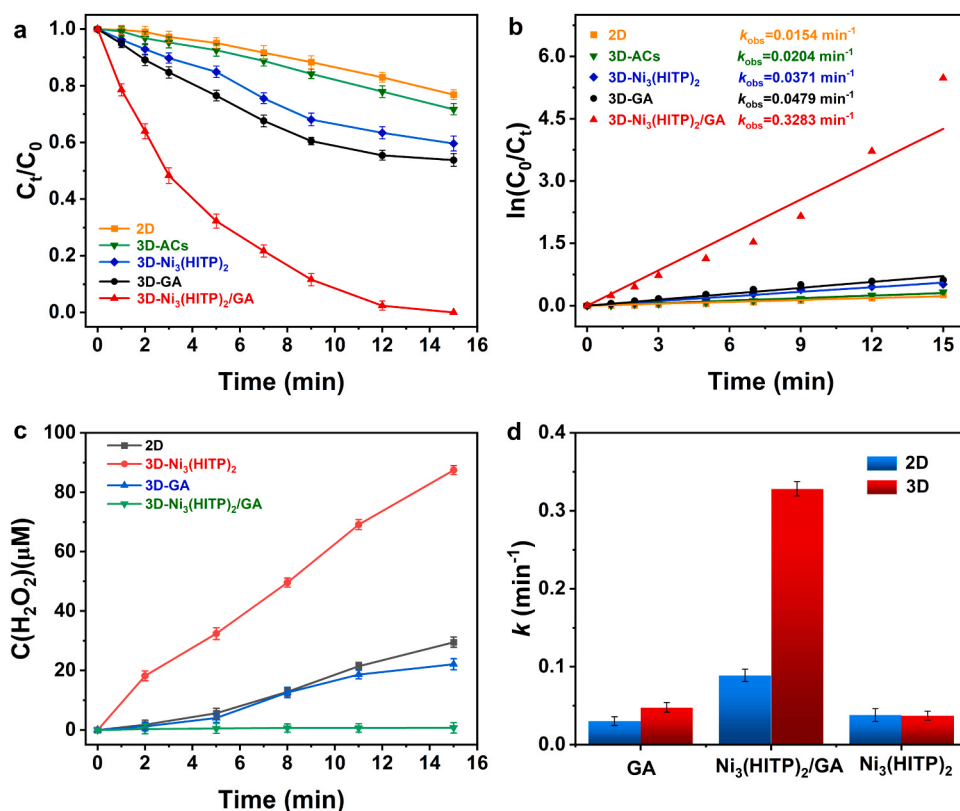

Fig. 5. (a) Degradation of phenol in different systems (2D represents the three-dimensional electrode system without any particle electrode added); (b) corresponding degradation rate constants; (c) amount of ●OH produced in different reaction systems under the same external H_2O_2 conditions; (d) corresponding degradation rate constants. (current density, 6 mA cm^{-2}; concentration of phenol in water, 50 ppm; catalyst dosage, 50 mg L^{-1}; pH 7.0; electrolyte (Na_2SO_4) concentration in water, 0.05 mol L^{-1}; air flow rate, 0.5 L min^{-1}).

the 2D electrode system was evaluated. A large gap exists between the degradation efficiency values of $Ni_3(HITP)_2$/GA and GA in the 2D electrode system and the 3D electrode system (Fig. 5(d)). Especially, for $Ni_3(HITP)_2$/GA, its decomposition rate constant ($0.0889 min^{-1}$) is about one-third that of the 2D electrode system. The main reason for this phenomenon is the microelectrode effect of the 3D electrode and the auxiliary effect of the two main electrode plates, resulting in a more efficient redox reaction [46]. Meanwhile, the adsorption performance of $Ni_3(HITP)_2$/GA towards phenol was assessed. An equilibrium adsorption capacity of $100.45 mg g^{-1}$ is reached within 200 min (Fig. S10(a), Table S3), providing a significant advantage over similar phenol adsorbents. However, the contribution of physical adsorption to phenol removal is only 5.9% within 15 min (Fig. S10(b)), which is far from the 3D degradation system established in this study. It indicates that the heterogeneous catalytic reaction of $Ni_3(HITP)_2$/GA particle electrode in presence of O_2 induces satisfactory phenol degradation. According to the above results, for the 3D in-situ self-electrolysis system, (1) phenol

molecules are enriched on electrode plate and on the particle electrode material with rich pore structure; (2) when potential is applied, hydrogen peroxide is generated at the cathode plate and also at $Ni_3(HITP)_2$ itself and the tetradentate $Ni–N_2O_2$ ligand bonding at the composite interface as $Ni_3(HITP)_2$/GA is polarized by electrostatic induction; (3) with the unique structure of $Ni_3(HITP)_2$/GA, the Fenton-like reaction of Ni and the $1e^-$ provided by microelectrode action takes place to convert H_2O_2 into •OH and achieve efficient degradation of pollutants.

In order to demonstrate the enhancement of H_2O_2 selectivity by the formation of $Ni–N_2O_2$ tetradentate coordination bonds in $Ni_3(HITP)_2$/GA particle electrode, the H_2O_2 selectivity of $Ni_3(HITP)_2$/GA, $Ni_3(HITP)_2$, and GA was compared (Fig. S11). The results show a significant increase in H_2O_2 selectivity for $Ni_3(HITP)_2$/GA compared with $Ni_3(HITP)_2$ and GA under the same conditions. This is mainly due to the formation of $Ni–N_2O_2$ tetradentate coordination bonds in $Ni_3(HITP)_2$/GA, which have been shown by researchers to contribute significantly to
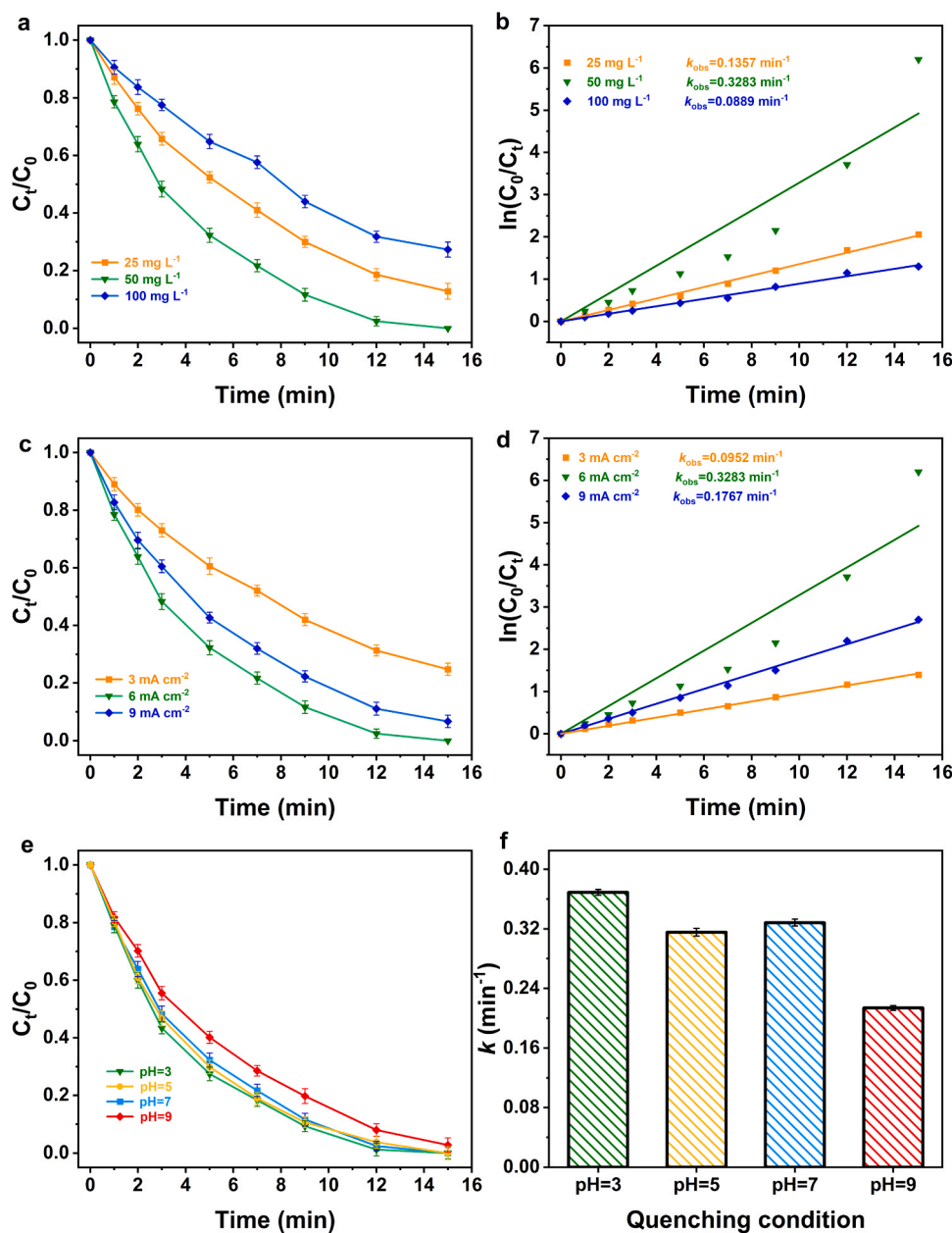

Fig. 6. (a, b) Effect of initial concentration of phenol; (c, d) effect of current density; (e, f) effect of pH (unless otherwise noted, current density, $6 mA cm^{-2}$; concentration of phenol in water, 50 ppm; catalyst dosage, $50 mg L^{-1}$; pH 7.0; electrolyte (Na_2SO_4) concentration in water, $0.05 mol L^{-1}$; air flow rate, $0.5 L min^{-1}$).

the improvement of H_2O_2 selectivity [47]. For the origin of the 1-electron that converts H_2O_2 to •OH, under the same external H_2O_2 conditions, the production of •OH in three systems was measured for 3D-Ni$_3$(HITP)$_2$/GA, 3D-Ni$_3$(HITP)$_2$, and 3D-GA, as shown in Fig. S12. The results show that 3D-Ni$_3$(HITP)$_2$/GA produces much more •OH than the other two systems at the same external H_2O_2. This result proves that the graphitic layer has the ability to produce 1-electrons only in the presence of Ni$_3$(HITP)$_2$. Owing to the graphite-like structure of Ni$_3$(HITP)$_2$, it can produce π-π charge off-domain effects with the graphene lamellae [27]. When Ni$_3$(HITP)$_2$ is encapsulated in the graphitic layer, the activated outgoing off-domain electrons are confined in such a narrow heterogeneous space, and under the action of electric field, H_2O_2 is converted into •OH in time.

3.2.1. Optimization of process parameters

The optimal conditions for the degradation of phenol in the 3D electrode system, such as the initial concentration of phenol, current density, and pH, were systematically explored to obtain the best organic pollutant removal. As shown in Fig. 6(a) and (b), as phenol concentration changes from 25 to 100 mg L^{-1}, the degradation efficiency of phenol increases first and then decreases. At low concentrations, the increase in pollutant concentration facilitates its diffusion to the electrode plate as well as the surface of the particle electrode, thus accelerating surface electrocatalytic reduction reaction [48]. However, when the concentration of phenol is too large, the ability of the system to electrolyze phenol cannot match the diffusion rate of phenol, resulting in a decrease in the degradation rate. Moreover, the higher the concentration of phenol, the more •OH is required for its full degradation. When the phenol concentration is too large, a large number of phenol molecules diffuse into the pore structure of the material, thus limiting the efficiency of •OH generation (Fig. S13(a)), and consequently, reducing the degradation efficiency of the system. Therefore, the optimal initial concentration of phenol is 50 mg L^{-1}.

The redox reactions occurring on the electrode surface and the polarization of the particle electrodes are driven by applied potential and current. Therefore, the magnitude of current seriously affects the degradation rate (Fig. 6(c) and (d)). With increasing current density, the degradation efficiency of phenol in the system increases first and then decreases. The decomposition rate constant also increases from 0.0952 min^{-1} to 0.3283 min^{-1} and then decreases to 0.1767 min^{-1}. Owing to increased current density, the driving force of the whole system becomes greater, particle electrodes are more likely to repolarize and produce microelectrolytic cells, and its redox effect is enhanced [49]. When the current density continues to increase, side reactions such as cathodic evolution of hydrogen and anodic evolution of oxygen occur [50], lowering the current efficiency and the •OH content in the system (Fig. S13(b)), thus affecting the electrocatalytic degradation process. Therefore, 6.0 mA cm^{-1} was chosen as the optimum current density. Meanwhile, as shown in Fig. S14, the COD value in the system decreases from the initial 178.34 mg L^{-1} to 43.38 mg L^{-1} after 15 min of reaction. According to energy consumption calculations, the system degrades phenol in 15 min with 0.53 kWh m^{-3} order^{-1}, corresponding to a specific energy consumption of 8.434 kWh kg^{-1} COD$_{phenol}^{-1}$. The system exhibits a surprising phenol degradation at a low energy consumption, indicating that the electrocatalytic process is an energy-efficient technology for the deep treatment of organic pollutants.

It is known that the initial pH of solution can seriously affect the electrocatalytic degradation of phenol, and most of the electrocatalytic degradation systems are Fenton and Fenton-like systems. These systems are dependent on acidic environment owing to the transformation of metal valence states, leading to their narrow application scope [51]. However, in this study, the degradation of phenol was tested at pH= 3, 5, 7, and 9. As shown in Fig. 6(e) and (f), the degradation rate of phenol exceeds 97% in 15 min at all pH values, and the corresponding decomposition rate constant exceeds 0.2 min^{-1}. Obviously, the system is extremely adaptable to both acidic and alkaline environments and

applicable to the treatment of coking wastewater with complex composition. This surprising effect is also due to the unique interface structure of Ni$_3$(HITP)$_2$/GA, which can provide 1e$^-$ for the conversion of H_2O_2 to •OH, thus reducing the dependence on acidic environment. Therefore, the pH of phenol solution was set at 7 as a starting point.

3.2.2. Cyclic stability of the system

The reusability of the 3D in-situ self-electrolysis system for Ni$_3$(HITP)$_2$/GA was investigated by continuous phenol degradation experiments. After the completion of each reaction, squeezing was conducted, followed by simple washing and drying through water and ethanol. As shown in Fig. 7(a), the removal rate of phenol could still reach 97.19% within 15 min after five consecutive degradation experiments, indicating the good reusability of Ni$_3$(HITP)$_2$/GA in the 3D in-situ self-electrolysis process for the degradation of organic pollutants. The amount of •OH produced during the five cycles does not change significantly (Fig. 7(b)), and the amount of •OH produced in the fifth cycle only differences from the first by 0.479 μM. In addition, as observed from the average voltage change of the system during the five cycles (Fig. 7(b)), the internal voltage remains basically unchanged, which ensures the system to continuously to work with low energy consumption and high efficiency. In addition, as shown in Fig. 7(c), the XRD patterns of the material after five cycles show that the characteristic peaks of Ni$_3$(HITP)$_2$ are still present. Meanwhile, for the post-reaction Ni$_3$(HITP)$_2$/GA, because of the rearrangement of crystalline structure, some new phases appear [52], while some peaks disappear, which may be due to falling off of the Ni$_3$(HITP)$_2$ particles attached to the surface of graphene oxide flakes in the continuous cycling experiments. This phenomenon also indicates that the Ni$_3$(HITP)$_2$ particles encapsulated by graphene oxide and coordinated with graphene oxide are stably bound, thus ensuring the good cycling performance of the material. This conclusion is also confirmed by the XPS maps of the material after cycling experiments, as seen in Fig. 7(d), where the content of elemental Ni slightly decreases after the cycling experiments. The high-resolution N 1 s and O 1 s plots of the material after cycling experiments show that Ni–N$_x$ and Ni–O peaks are still present, which is consistent with the above XRD results. The Ni (II) (Ni–N$_2$O$_2$)/Ni (II) (Ni–N$_4$) ratio in the material is significantly elevated after the cyclic reaction (Fig. S15, Table S4). We presume that it is the large retention of Ni–N$_2$O$_2$ that allows the material to maintain its excellent degradation performance after a large structural damage. These results also suggest that the striking degradation effect of Ni$_3$(HITP)$_2$/GA may be produced by the combination of the Ni$_3$(HITP)$_2$ particles encapsulated inside the graphene oxide and the special four-dentate coordination bonds formed by the graphene oxide and Ni$_3$(HITP)$_2$.

3.2.3. Degradation mechanism and pathway of phenol in the 3D in-situ self-electrolysis system

To investigate the effect of active radical species on the phenol removal efficiency of the Ni$_3$(HITP)$_2$/GA-based 3D in-situ self-electrolysis system, the reactive radicals generated during the reaction were identified by radical quenching experiments. As shown in Fig. 8(a) and (b), when methanol (the radical scavenger of SO$_4^{•-}$) is added to the reactant mixture, the phenol degradation rate of the system as well as the decomposition rate constant do not change significantly, indicating that SO$_4^{•-}$ is not the reactive species of the system [53]. However, when TBA (a radical scavenger of •OH) is added to the reactants, the phenol degradation efficiency is decreased significantly and the reaction is nearly quenched, indicating the dominant role by the reactive species •OH in the degradation of phenol in the system [54]. Meanwhile, the reaction is also inhibited to some extent after the addition of chloroform (a radical scavenger of O$_2^{•-}$), indicating the presence of O$_2^{•-}$ active species in the system [55]. Electron Paramagnetic Resonance (EPR) test shows the distinct signals of DMPO-•OH and DMPO-O$_2^{•-}$ complexes in the 3D-Ni$_3$(HITP)$_2$/GA system(Fig. 8(c), Fig. S16). This result indicates that a large number of •OH and O$_2^{•-}$ active species are present in the
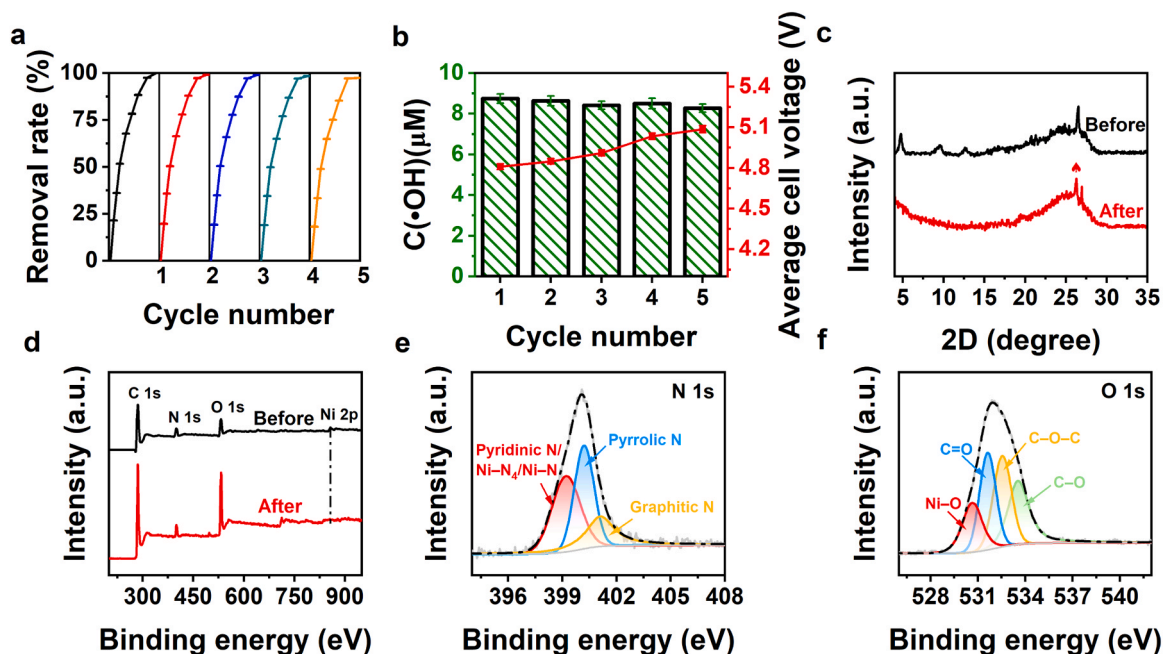
Fig. 7. (a) Phenol degradation rate in five-cycle experiment; (b) amount of •OH production and the change of the average voltage of the system during five cycles of experiment; (c) XRD patterns, (d) X-ray photoelectron spectra, (e)N 1 s, and (f) O 1 s spectra of Ni$_3$(HITP)$_2$/GA after five-cycle experiment (current density, 6 mA cm^{-2}; concentration of phenol in water, 50 ppm; catalyst dosage, 50 mg L^{-1}; pH 7.0; electrolyte (Na$_2$SO$_4$) concentration in water, 0.05 mol L^{-1}; air flow rate, 0.5 L min^{-1}).
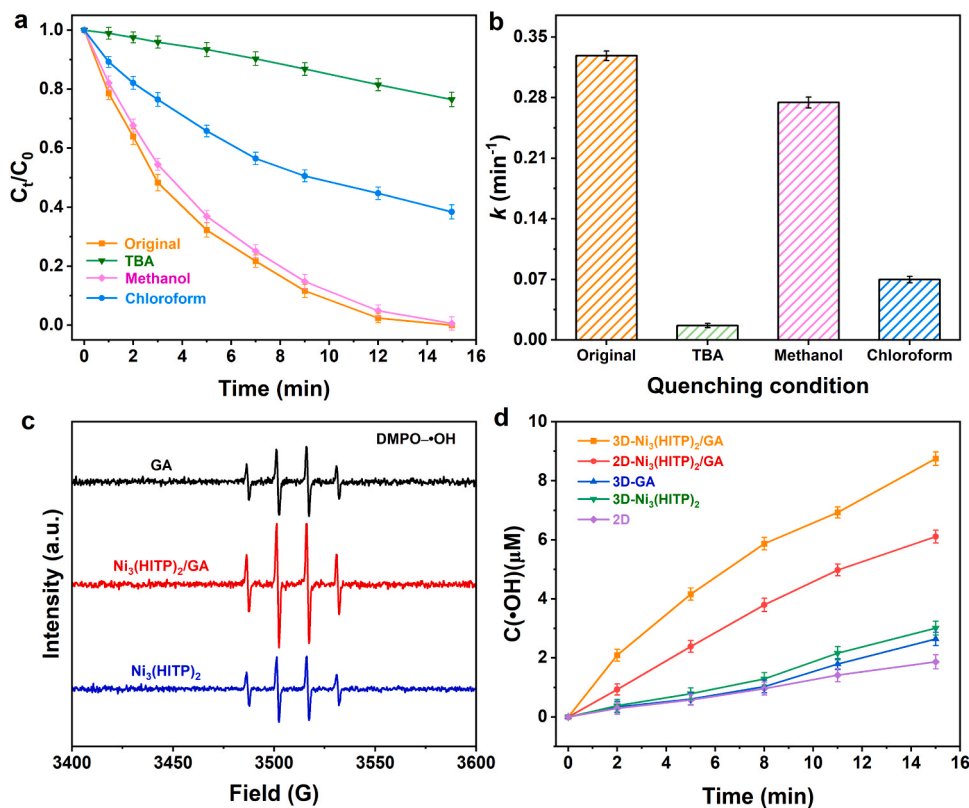
Fig. 8. (a) Comparison of the degradation effect of different quenching conditions; (b) corresponding comparison of the reaction rates; (c) EPR spectra of •OH captured by DMPO (d) amount of •OH produced in different reaction systems (current density, 6 mA cm^{-2}; concentration of phenol in water, 50 ppm; catalyst dosage, 50 mg L^{-1}; pH 7.0; electrolyte (Na$_2$SO$_4$) concentration in water, 0.05 mol L^{-1}; air flow rate, 0.5 L min^{-1}; TBA, 0.5 M; Methanol, 0.5 M; Chloroform, 0.5 M).
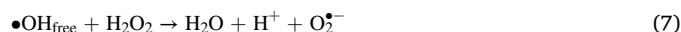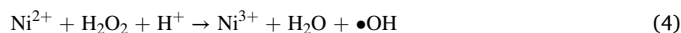
3D-Ni$_3$(HITP)$_2$/GA degradation system. According to these findings, it can be concluded that in the 3D electrode system, phenol removal is dominated by ●OH and O$_2^{\bullet-}$.

In Fig. 8(d), 7-hydroxycoumarin was measured in response to a reaction between ●OH and coumarin to see whether the concentration of ●OH in the reaction changed with increasing reaction time. 3D-Ni$_3$(HITP)$_2$/GA system produces a large amount of ●OH rapidly within 15 min with the maximum concentration of 8.75 μM. Meanwhile, 3D-Ni$_3$(HITP)$_2$, 3D-GA, and 2D systems also produce ●OH within 15 min of the catalytic reaction, but at much lower concentrations than 3D-Ni$_3$(HITP)$_2$/GA system. As shown in Fig. 8(c), though DMPO-●OH signals were also detected in the 3D-Ni$_3$(HITP)$_2$ and 3D-GA system, significantly stronger DMPO-●OH signals were detected in the 3D-Ni$_3$(HITP)$_2$/GA system. The experimental results are consistent with the phenol degradation in these reaction systems, which proves that the electrocatalytic degradation process is dependent upon ●OH, and the main reason for the efficient and deep phenol degradation ability of the 3D-Ni$_3$(HITP)$_2$/GA system is the efficient generation of ●OH. It is noteworthy that though 3D-Ni$_3$(HITP)$_2$ produces a higher concentration of ●OH in 15 min compared with 3D-GA, its degradation is not as effective. 3D-Ni$_3$(HITP)$_2$ produces a higher concentration of ●OH probably because of its strong hydrogen peroxide production ability, and a large amount of hydrogen peroxide produces relatively more ●OH under its own moderate Fenton-like effect. However, when GA is used as a 3D material with rich pore structure, the abundant pores in its structure, the dangling –COOH on the graphene oxide lamellae, and the internal defects provide strong motivation for the adsorption of O$_2$ as well as the transport of electrons [56]. Thus, its easy generation of O$_2^{\bullet-}$ through O$_2$-binding electrons is rationalizable. As shown in Fig. S17(a), the phenol degradation reaction is also inhibited to some extent in the 3D-GA system after the addition of chloroform (a radical scavenger for O$_2^{\bullet-}$), and therefore O$_2^{\bullet-}$ active specie is present in this system. In contrast, the 3D-Ni$_3$(HITP)$_2$ system shows almost no change in the degradation of phenol after the addition of the same quenching agent (Fig. S17(b)). Meanwhile, EPR test shows that the DMPO-O$_2^{\bullet-}$ signal was only present in the 3D-GA system, and it was not detected in the 3D-Ni$_3$(HITP)$_2$ system (Fig. S16). The results also indicate that O$_2^{\bullet-}$ active specie in the 3D electrode system is mainly produced by GA, so that the surprising effect exhibited by the 3D-Ni$_3$(HITP)$_2$/GA system is produced by the interaction of each part of the system, in which each component is indispensable.

According to the experimental results and discussion mentioned

Fig. 9. Mechanism of phenol removal from coking wastewater by a Ni$_3$(HITP)$_2$/GA-based 3D in-situ self-electrolysis system.

above, the mechanism of the 3D in-situ self-electrolysis system based on Ni$_3$(HITP)$_2$/GA for the removal of phenol from coking wastewater is proposed. As shown in Fig. 9, oxygen from the air enters the solution and diffuses to the stainless steel cathode as well as to the surface of the particle electrode to generate H$_2$O$_2$ through the 2e$^-$ ORR path (Eq. (2)). The unique ligand structure of Ni$_3$(HITP)$_2$ and the tetradentate Ni–N$_2$O$_2$ coordination bond at the interface of the composite material exist inside Ni$_3$(HITP)$_2$/GA as a particle electrode, and the presence of these structures enables the highly selective in-situ generation of large amounts of H$_2$O$_2$ in the material itself. At the same time, the abundant oxygen-containing functional groups on Ni$_3$(HITP)$_2$/GA are conducive to the adsorption of O$_2$ during the reaction process, and the large number of pore structures is conducive to the improvement of the electron transfer efficiency [57,58]. Therefore, the abundant oxygen-containing functional groups and a large number of pore structures in Ni$_3$(HITP)$_2$/GA enhance the oxidation for water, improve the selectivity of 2e$^-$ reduction for O$_2$, and reduce the self-decomposition rate of H$_2$O$_2$, thus increasing H$_2$O$_2$ yield [59]. In addition, the defects on the graphene oxide sheet layer also facilitate the adsorption of O$_2$ by the system. After H$_2$O$_2$ production, the reaction system converts H$_2$O$_2$ to ●OH synergistically by microelectrode action, activated graphene electrocatalytic activity, and Fenton-like effect of Ni (Eqs. (3–5)). In addition, part of the O$_2$ adsorbed on the surface of the particle electrode is converted to O$_2^{\bullet-}$ after combining the e$^-$ provided by the microelectrode (Eq. (6)), and part of free ●OH interacts with H$_2$O$_2$ to form O$_2^{\bullet-}$ (Eq. (7)). Under the joint attack of ●OH and O$_2^{\bullet-}$, the phenol molecules adsorbed on the surface of Ni$_3$(HITP)$_2$/GA are mineralized into small molecules such as CO$_2$ and H$_2$O.

$$O_2 + 2\,H^+ + 2e^- \rightarrow H_2O_2 \tag{2}$$

$$H_2O_2 + e^-_{\ carbon} \rightarrow \bullet OH + OH^- \tag{3}$$

$$Ni^{2+} + H_2O_2 + H^+ \rightarrow Ni^{3+} + H_2O + \bullet OH \tag{4}$$

$$Ni^{3+} + e^- \rightarrow Ni^{2+} \tag{5}$$

$$O_2 + e^- \rightarrow O_2^{\bullet-} \tag{6}$$

$$\bullet OH_{free} + H_2O_2 \rightarrow H_2O + H^+ + O_2^{\bullet-} \tag{7}$$

The degradation of phenol in this system is superior in terms of degradation rate and efficiency over numerous 3D-electrode degradation systems in the literature so far (Table S5). The surprising results of this study are all attributed to the establishment of a 3D in-situ self-electrolysis system, which is based on a 3D electrode with a material as a particle electrode. This particle electrode has the ability to generate H$_2$O$_2$ using its internal Ni$_3$(HITP)$_2$ and the Ni–N$_2$O$_2$ tetradentate coordination bond formed at the internal interface of the material, and to convert H$_2$O$_2$ to ●OH in situ through its own graphite shell structure.

The degradation intermediates at different times were detected by GC-MS as shown in Fig. S18. From GC-MS, benzoquinone, hydroquinone, catechol, and maleic anhydride appeared during the degradation process [60]. The sample needs to be dehydrated for GC-MS testing, and maleic acid dehydrates to form maleic anhydride. Thus, we proposed a plausible degradation pathway for phenol in the system (Fig. S19). Owing to the electron-withdrawing effect of phenol, hydroquinone and catechol are formed at first in the presence of ●OH [61]. And with the continued attack of ●OH, hydroquinone and catechol are converted to *p*-benzoquinone. Meanwhile, some *p*-benzoquinone is also formed owing to the oxidation of phenol when it is attacked by O$_2^{\bullet-}$. Then, with the continued attack of free radicals, the ring-opening of *p*-benzoquinone is obtained to form carboxylic acids, which are eventually converted to CO$_2$ and H$_2$O [50].

4. Conclusion
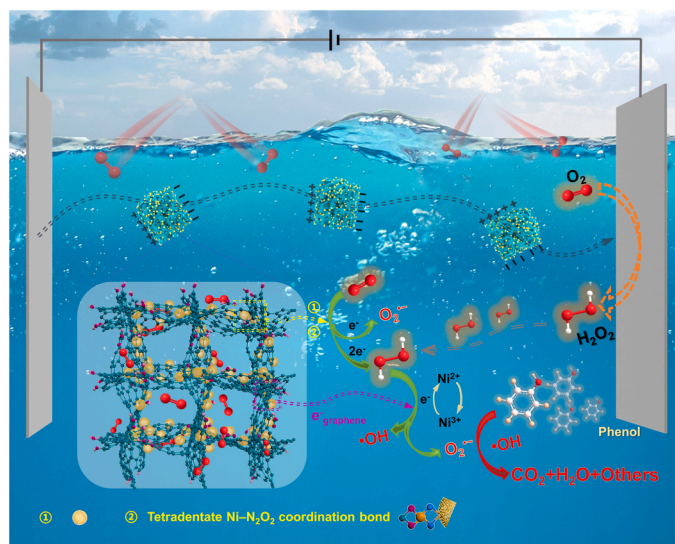
In summary, a Ni$_3$(HITP)$_2$/graphene-based composite aerogel

particle electrode with high electrical conductivity and high catalytic activity was developed by self-assembly technology, and a 3D in-situ self-electrolysis system with efficient phenol degradation capability was established with this particle electrode. In this system, the $Ni_3(HITP)_2$ in $Ni_3(HITP)_2$/GA and the tetradentate $Ni–N_2O_2$ coordination bond formed at the interface of the composite material generate H_2O_2 with high selectivity and in-situ through the $2e^-$ pathway, and the graphene layer converts H_2O_2 into •OH by using the $1e^-$ transfer of $Ni_3(HITP)_2$ excitation and the microelectrode action of the particle electrode. At the same time, the system uses •OH (graphene layers' $1e^-$ action) and $O_2^{•-}$ action (enriched O_2) together to significantly reduce the dependence on acidic environment and broaden its utilization range. After 5 cycles of degradation, the system maintained 97.19% of its initial degradation rate with good durability. The 3D in-situ self-electrolysis system based on $Ni_3(HITP)_2$/GA particle electrodes has a surprisingly efficient degradation of phenol and is expected to achieve practical application in coking wastewater. This work provides a new strategy for the efficient use of particle electrodes in 3D electrodes and expands the application of 3D electrodes in the field of deep treatment of organic matter in coking wastewater.

CRediT authorship contribution statement

Shaojun Gao: Methodology, Validation, Formal analysis, Investigation, Data Curation, Writing-Original draft preparation, Visualization. **Weifeng Liu:** Conceptualization, Validation, Investigation, Resources, Writing-Reviewing and Editing, Visualization, Supervision, Project administration, Funding acquisition. **Meiling Wang:** Resources, Supervision. **Zongbin Zhao** : Conceptualization, Writing-Reviewing. **Xuguang Liu** : Conceptualization, Validation, Investigation, Resources, Writing-Reviewing and Editing, Visualization, Supervision, Project administration, Funding acquisition.

Declaration of Competing Interest

The authors declare that they have no known competing financial interests or personal relationships that could have appeared to influence the work reported in this paper.

Data availability

Data will be made available on request.

Acknowledgements

Appendix A. Supplementary material

Supplementary data associated with this article can be found in the online version at doi:10.1016/j.apcatb.2023.123276.

References

[1] Q. Gao, P. Jin, L. Wang, Y. Xing, X. Gui, P. Van Puyvelde, B. Van der Bruggen, Removal of organic pollutants in coking wastewater based on coal-based adsorbents: A pilot-scale study of static adsorption and flotation, J. Environ. Chem. Eng. 9 (2021), 106844, https://doi.org/10.1016/j.jece.2021.106844.
[2] J. Zhang, L. Qin, Y. Yang, X. Liu, Porous carbon nanospheres aerogel based molecularly imprinted polymer for efficient phenol adsorption and removal from wastewater, Sep. Purif. Technol. 274 (2021), 119029, https://doi.org/10.1016/j.seppur.2021.119029.
[3] W. An, H. Wang, T. Yang, J. Xu, Y. Wang, D. Liu, J. Hu, W. Cui, Y. Liang, Enriched photocatalysis-Fenton synergistic degradation of organic pollutants and coking wastewater via surface oxygen vacancies over Fe-BiOBr composites, Chem. Eng. J. 451 (2023), 138653, https://doi.org/10.1016/j.cej.2022.138653.
[4] Y. Wang, Z. Zhang, Z. Yin, Z. Liu, Y. Liu, Z. Yang, W. Yang, Adsorption and catalysis of peroxymonosulfate on carbocatalysts for phenol degradation: The role of pyrrolic-nitrogen, Appl. Catal. B Environ. 319 (2022), 121891, https://doi.org/10.1016/j.apcatb.2022.121891.
[5] F. Gao, H. Lyu, S. Ahmad, S. Xu, J. Tang, Enhanced reductive degradation of tetrabromobisphenol A by biochar supported sulfidated nanoscale zero-valent iron: Selectivity and core reactivity, Appl. Catal. B Environ. 324 (2023), 122246, https://doi.org/10.1016/j.apcatb.2022.122246.
[6] C. Zhang, Y. Jiang, Y. Li, Z. Hu, L. Zhou, M. Zhou, Three-dimensional electrochemical process for wastewater treatment: A general review, Chem. Eng. J. 228 (2013) 455–467, https://doi.org/10.1016/j.cej.2013.05.033.
[7] W. Sun, Y. Sun, K.J. Shah, P.-C. Chiang, H. Zheng, Electrocatalytic oxidation of tetracycline by Bi-Sn-Sb/γ-Al2O3 three-dimensional particle electrode, J. Hazard. Mater. (2018) 24–32, https://doi.org/10.1016/j.jhazmat.2018.09.085.
[8] T. Wang, Y. Song, H. Ding, Z. Liu, A. Baldwin, I. Wong, H. Li, C. Zhao, Insight into synergies between ozone and in-situ regenerated granular activated carbon particle electrodes in a three-dimensional electrochemical reactor for highly efficient nitrobenzene degradation, Chem. Eng. J. 394 (2020), 124852, https://doi.org/10.1016/j.cej.2020.124852.
[9] B. Song, Z. Wang, J. Li, M. Luo, P. Cao, C. Zhang, Volcanic rock: A new type of particle electrode with excellent performance, which can efficiently degrade norfloxacin, Chem. Eng. J. 426 (2021), 131940, https://doi.org/10.1016/j.cej.2021.131940.
[10] W. Zhang, Y. He, C. Li, X. Hu, S. Yang, X. You, W. Liang, Persulfate activation using Co/AC particle electrodes and synergistic effects on humic acid degradation, Appl. Catal. B: Environ. 285 (2021), 119848, https://doi.org/10.1016/j.apcatb.2020.119848.
[11] B. Shi, L. Zhang, H. Sun, J. Ren, H. Wang, H. Tang, Z. Bian, Efficient and recyclable Ni-Ce-Mn-N modified ordered mesoporous carbon electrode during electrocatalytic ozonation process for the degradation of simulated high-salt phenol wastewater, Chemosphere 304 (2022), 135258, https://doi.org/10.1016/j.chemosphere.2022.135258.
[12] H. Ghanbarlou, B. Nasernejad, M.N. Fini, M.E. Simonsen, J. Muff, Synthesis of an iron-graphene based particle electrode for pesticide removal in three-dimensional heterogeneous electro-Fenton water treatment system, Chem. Eng. J. 395 (2020), 125025, https://doi.org/10.1016/j.cej.2020.125025.
[13] Y. Wu, Z. Gao, Y. Feng, Q. Cui, C. Du, C. Yu, L. Liang, W. Zhao, J. Feng, J. Sun, R. Yang, J. Sun, Harnessing selective and durable electrosynthesis of H2O2 over dual-defective yolk-shell carbon nanosphere toward on-site pollutant degradation, Appl. Catal. B Environ. 298 (2021), 120572, https://doi.org/10.1016/j.apcatb.2021.120572.
[14] S. Ma, D. Yang, Y. Guan, Y. Yang, Y. Zhu, Y. Zhang, J. Wu, L. Sheng, L. Liu, T. Yao, Maximally exploiting active sites on Yolk@shell nanoreactor: Nearly 100% PMS activation efficiency and outstanding performance over full pH range in Fenton-like reaction, Appl. Catal. B: Environ. 316 (2022), 121594, https://doi.org/10.1016/j.apcatb.2022.121594.
[15] D. Xing, Z. Cui, Y. Liu, Z. Wang, P. Wang, Z. Zheng, H. Cheng, Y. Dai, B. Huang, Two-dimensional π–d conjugated metal–organic framework Fe3(hexaiminotriphenylene)2 as a photo-Fenton like catalyst for highly efficient degradation of antibiotics, Appl. Catal. B Environ. (2021), 120029, https://doi.org/10.1016/j.apcatb.2021.120029.
[16] D. Xing, Y. Wang, P. Zhou, Y. Liu, Z. Wang, P. Wang, Z. Zheng, H. Cheng, Y. Dai, B. Huang, Co3(hexaiminotriphenylene)2: A conductive two-dimensional π–d conjugated metal–organic framework for highly efficient oxygen evolution reaction, Appl. Catal. B: Environ. (2020), 119295, https://doi.org/10.1016/j.apcatb.2020.119295.
[17] E.M. Miner, T. Fukushima, D. Sheberla, L. Sun, Y. Surendranath, M. Dinca, Electrochemical oxygen reduction catalysed by Ni3(hexaiminotriphenylene)2, Nat. Commun. 7 (2016) 10942, https://doi.org/10.1038/ncomms10942.
[18] F. Xiao, Z. Wang, J. Fan, T. Majima, H. Zhao, G. Zhao, Selective electrocatalytic reduction of oxygen to hydroxyl radicals via 3-electron pathway with FeCo alloy encapsulated carbon aerogel for fast and complete removing pollutants, Angew. Chem. Int. Ed. 60 (2021) 10375–10383, https://doi.org/10.1002/anie.202101804.
[19] B. Huang, Y. Liu, B. Li, S. Liu, G. Zeng, Z. Zeng, X. Wang, Q. Ning, B. Zheng, C. Yang, Effect of Cu(II) ions on the enhancement of tetracycline adsorption by Fe3O4@SiO2-Chitosan/graphene oxide nanocomposite, Carbohydr. Polym. 157 (2017) 576–585, https://doi.org/10.1016/j.carbpol.2016.10.025.
[20] H. Hu, Z. Zhao, W. Wan, Y. Gogotsi, J. Qiu, Ultralight and highly compressible graphene aerogels, Adv. Mater. 25 (2013) 2219–2223, https://doi.org/10.1002/adma.201204530.
[21] X. Wang, Y. Zhuang, B. Shi, Degradation of trichloroacetic acid by MOFs-templated CoFe/graphene aerogels in peroxymonosulfate activation, Chem. Eng. J. 450 (2022), 137799, https://doi.org/10.1016/j.cej.2022.137799.
[22] N. Diez, M. Qiao, J. Luis Gomez-Urbano, C. Botas, D. Carriazo, M.M. Titirici, High density graphene-carbon nanosphere films for capacitive energy storage, J. Mater. Chem. A 7 (2019) 6126–6133, https://doi.org/10.1039/C8TA12050A.
[23] F. Sun, X. Chen, Oxygen reduction reaction on Ni3(HITP)2: A catalytic site that leads to high activity, Electrochem. Commun. 82 (2017) 89–92, https://doi.org/10.1016/j.elecom.2017.07.028.

[24] X. Chen, S. Huang, F. Sun, N. Lai, Modifications of metal and ligand to modulate the oxygen reduction reaction activity of two-dimensional MOF catalysts, J. Phys. Chem. C. 124 (2020) 1413–1420, https://doi.org/10.1021/acs.jpcc.9b09647.

[25] J.M. Yoo, H. Shin, D.Y. Chung, Y.E. Sung, Carbon shell on active nanocatalyst for stable electrocatalysis, Acc. Chem. Res. 55 (2022) 1278–1289, https://doi.org/10.1021/acs.accounts.1c00727.

[26] H.S. Su, H.S. Feng, Q.Q. Zhao, X.G. Zhang, J.J. Sun, Y. He, S.C. Huang, T.X. Huang, J.H. Zhong, D.Y. Wu, B. Ren, Probing the local generation and diffusion of active oxygen species on a Pd/Au bimetallic surface by tip-enhanced raman spectroscopy, J. Am. Chem. Soc. 142 (2020) 1341–1347, https://doi.org/10.1021/jacs.9b10512.

[27] Q. Mu, W. Zhu, X. Li, C. Zhang, Y. Su, Y. Lian, P. Qi, Z. Deng, D. Zhang, S. Wang, X. Zhu, Y. Peng, Electrostatic charge transfer for boosting the photocatalytic CO_2 reduction on metal centers of 2D MOF/rGO heterostructure, Appl. Catal. B Environ. 262 (2020), 118144, https://doi.org/10.1016/j.apcatb.2019.118144.

[28] M. Lu, G. Wang, X. Yang, B. Hou, In situ growth CNT@MOFs core-shell structures enabling high specific supercapacitances in neutral aqueous electrolyte, Nano Res. 15 (2022) 6112–6120, https://doi.org/10.1007/s12274-022-4184-y.

[29] W. Kang, Y. Cui, Y. Yang, Z. Zhao, X. Wang, X. Liu, An acid induction strategy to construct an ultralight and durable amino-functionalized graphene oxide aerogel for enhanced quinoline pollutants extraction from coking wastewater, Chem. Eng. J. 412 (2021), 128686, https://doi.org/10.1016/j.cej.2021.128686.

[30] W. Kang, Y. Cui, L. Qin, Y. Yang, Z. Zhao, X. Wang, X. Liu, A novel robust adsorbent for efficient oil/water separation: Magnetic carbon nanospheres/graphene composite aerogel, J. Hazard. Mater. 392 (2020), 122499, https://doi.org/10.1016/j.jhazmat.2020.122499.

[31] C. Li, J. Yang, P. Pachfule, S. Li, M.-Y. Ye, J. Schmidt, A. Thomas, Ultralight covalent organic framework/graphene aerogels with hierarchical porosity, Nat. Commun. 11 (2020) 4712, https://doi.org/10.1038/s41467-020-18427-3.

[32] H. Zeng, Z. Yu, L. Shao, X. Li, M. Zhu, Y. Liu, X. Feng, X. Zhu, A novel strategy for enhancing the performance of membranes for dyes separation: Embedding PAA@ UiO-66-NH_2 between graphene oxide sheets, Chem. Eng. J. 403 (2021), 126281, https://doi.org/10.1016/j.cej.2020.126281.

[33] S. Liu, S. Yin, Z. Zhang, L. Feng, Y. Liu, L. Zhang, Regulation of defects and nitrogen species on carbon nanotube by plasma-etching for peroxymonosulfate activation: Inducing non-radical/ radical oxidation of organic contaminants, J. Hazard. Mater. 441 (2023), 129905, https://doi.org/10.1016/j.jhazmat.2022.129905.

[34] W. Peng, J. Liu, X. Liu, L. Wang, L. Yin, H. Tan, F. Hou, J. Liang, Facilitating two-electron oxygen reduction with pyrrolic nitrogen sites for electrochemical hydrogen peroxide production, Nat. Commun. 14 (2023) 4430, https://doi.org/10.1038/s41467-023-40118-y.

[35] S. Chen, T. Luo, X. Li, K. Chen, J. Fu, K. Liu, C. Cai, Q. Wang, H. Li, Y. Chen, C. Ma, L. Zhu, Y.R. Lu, T.S. Chan, M. Zhu, E. Cortés, M. Liu, Identification of the highly active Co–N_4 coordination motif for selective oxygen reduction to hydrogen peroxide, J. Am. Chem. Soc. 144 (2022) 14505–14516, https://doi.org/10.1021/jacs.2c01194.

[36] W.W. Tian, J.T. Ren, X.W. Lv, Z.Y. Yuan, A "gas-breathing" integrated air diffusion electrode design with improved oxygen utilization efficiency for high-performance Zn-air batteries, Chem. Eng. J. 431 (2022), 133210, https://doi.org/10.1016/j.cej.2021.133210.

[37] Y. Wu, Y. Ding, X. Han, B. Li, Y. Wang, S. Dong, Q. Li, S. Dou, J. Sun, J. Sun, Modulating coordination environment of Fe single atoms for high-efficiency all-pH-tolerated H_2O_2 electrochemical production, Appl. Catal. B Environ. 315 (2022), 121578, https://doi.org/10.1016/j.apcatb.2022.121578.

[38] W. Zhu, C. Zhang, Q. Li, L. Xiong, R. Chen, X. Wan, Z. Wang, W. Chen, Z. Deng, Y. Peng, Selective reduction of CO_2 by conductive MOF nanosheets as an efficient co-catalyst under visible light illumination, Appl. Catal. B Environ. 238 (2018) 339–345, https://doi.org/10.1016/j.apcatb.2018.07.024.

[39] W. Yang, N.N. Wang, P. Ping, A.C.Y. Yuen, A. Li, S.E. Zhu, L.L. Wang, J. Wu, T.B. Y. Chen, J.Y. Si, B.D. Rao, H.D. Lu, Q.N. Chan, G.H. Yeoh, Novel 3D network architectured hybrid aerogel comprising epoxy, graphene, and hydroxylated boron nitride nanosheets, ACS Appl. Mater. Interfaces 10 (2018) 40032–40043, https://doi.org/10.1021/acsami.8b15301.

[40] Y. Shiraishi, Y. Kofuji, H. Sakamoto, S. Tanaka, S. Ichikawa, T. Hirai, Effects of surface defects on photocatalytic H_2O_2 production by mesoporous graphitic carbon nitride under visible light irradiation, ACS Catal. 5 (2015) 3058–3066, https://doi.org/10.1021/acscatal.5b00408.

[41] W. Zhao, T. Chen, W. Wang, B. Jin, J. Peng, S. Bi, M. Jiang, S. Liu, Q. Zhao, W. Huang, Conductive $Ni_3(HITP)_2$ MOFs thin films for flexible transparent supercapacitors with high rate capability, Sci. Bull. 65 (2020) 1803–1811, https://doi.org/10.1016/j.scib.2020.06.027.

[42] G. Zhang, J. Hu, Y. Nie, Y. Zhao, L. Wang, Y. Li, H. Liu, L. Tang, X. Zhang, D. Li, L. Sun, H. Duan, Integrating flexible ultralight 3D Ni micromesh current collector with NiCo bimetallic hydroxide for smart hybrid supercapacitors, Adv. Funct. Mater. 31 (2021) 2100290, https://doi.org/10.1002/adfm.202100290.

[43] G. Gan, X. Zhang, S. Bu, Q. Gao, X. Kong, Y. Lei, A. Zhu, K. Liu, C. Luan, T. Zhang, Y. Li, C.-S. Lee, W. Zhang, Metal-nitrogen-carbon single-atom aerogels as self-supporting electrodes for dechlorination of 1,2-dichloroethane, Adv. Funct. Mater. (2022) 2206263, https://doi.org/10.1002/adfm.202206263.

[44] Q. Yu, X. Liu, G. Liu, X. Wang, Z. Li, B. Li, Z. Wu, L. Wang, Constructing three-phase heterojunction with 1D/3D hierarchical structure as efficient trifunctional

[45] K.Y. Park, M.E. Swers, U. Berner, E. Hirth, J.R. Downing, J. Hui, J. Mailoa, C. Johnston, S. Kim, L.C. Seitz, M.C. Hersam, Mitigating Pt loss in polymer electrolyte membrane fuel cell cathode catalysts using graphene nanoplatelet pickering emulsion processing, Adv. Funct. Mater. (2022) 2205216, https://doi.org/10.1002/adfm.202205216.

[46] Y. Lian, W. Yang, C. Zhang, H. Sun, Z. Deng, W. Xu, L. Song, Z. Ouyang, Z. Wang, J. Guo, Y. Peng, Unpaired 3d electrons on atomically dispersed cobalt centres in coordination polymers regulate both oxygen reduction reaction (ORR) activity and selectivity for use in zinc-air batteries, Angew. Chem. Int. Ed. 59 (2020) 286–294, https://doi.org/10.1002/anie.201910879.

[47] Y. Wang, R. Shi, L. Shang, G.I.N. Waterhouse, J. Zhao, Q. Zhang, L. Gu, T. Zhang, High-efficiency oxygen reduction to hydrogen peroxide catalyzed by nickel single-atom catalysts with tetradentate N_2O_2 coordination in a three-phase flow cell, Angew. Chem. Int. Ed. 59 (2020) 13057–13062, https://doi.org/10.1002/anie.202004841.

[48] X. Fu, Y. Han, H. Xu, Z. Su, L. Liu, Electrochemical study of a novel high-efficiency PbO_2 anode based on a cerium-graphene oxide co-doping strategy: Electrodeposition mechanism, parameter optimization, and degradation pathways, J. Hazard. Mater. 422 (2022), 126890, https://doi.org/10.1016/j.jhazmat.2021.126890.

[49] J. Yu, J. Zou, P. Xu, Q. He, Three-dimensional photoelectrocatalytic degradation of the opaque dye acid fuchsin by Pr and Co co-doped TiO_2 particle electrodes, J. Clean. Prod. 251 (2020), 119744, https://doi.org/10.1016/j.jclepro.2019.119744.

[50] Q. Zhou, D. Liu, G. Yuan, Y. Tang, K. Cui, S. Jang, Y. Xia, W. Xiong, Efficient degradation of phenolic wastewaters by a novel Ti/PbO_2-Cr-PEDOT electrode with enhanced electrocatalytic activity and chemical stability, Sep. Purif. Technol. 281 (2022), 119735, https://doi.org/10.1016/j.seppur.2021.119735.

[51] Y. Jiang, P. Ni, C. Chen, Y. Lu, P. Yang, B. Kong, A. Fisher, X. Wang, Selective electrochemical H_2O_2 production through two-electron oxygen electrochemistry, Adv. Energy Mater. 8 (2018) 1801909, https://doi.org/10.1002/aenm.201801909.

[52] D. Sheberla, L. Sun, M.A. Blood-Forsythe, S. Er, C.R. Wade, C.K. Brozek, A. Aspuru-Guzik, M. Dincă, High electrical conductivity in $Ni_3(2,3,6,7,10,11$-hexaiminotriphenylene)$_2$, a semiconducting metal–organic graphene analogue, J. Am. Chem. Soc. 136 (2014) 8859–8862, https://doi.org/10.1021/ja502765n.

[53] X. Li, X. Huang, S. Xi, S. Miao, J. Ding, W. Cai, S. Liu, X. Yang, H. Yang, J. Gao, J. Wang, Y. Huang, T. Zhang, B. Liu, Single cobalt atoms anchored on porous N-doped graphene with dual reaction sites for efficient fenton-like catalysis, J. Am. Chem. Soc. 140 (2018) 12469–12475, https://doi.org/10.1021/jacs.8b05992.

[54] L. Wang, D. Ding, Z. Qian, M. Dzakpasu, R. Chen, G. Wang, S. Yang, Intensification of van der Waals interaction for efficient peroxymonosulfate activation and accuracy re-evaluation of quenching experiments for reactive oxidation species identification, Chem. Eng. J. 450 (2022), 138353, https://doi.org/10.1016/j.cej.2022.138353.

[55] W. Huang, M. Brigante, F. Wu, C. Mousty, K. Hanna, G. Mailhot, Assessment of the Fe(III)-EDDS complex in fenton-like processes: from the radical formation to the degradation of bisphenol A, Environ. Sci. Technol. 47 (2013) 1952–1959, https://doi.org/10.1021/es304502y.

[56] C. Tang, Y. Jiao, B. Shi, J.-N. Liu, Z. Xie, X. Chen, Q. Zhang, S.Z. Qiao, Coordination tunes selectivity: two-electron oxygen reduction on high-loading molybdenum single-atom catalysts, Angew. Chem. Int. Ed. 59 (2020) 9171–9176, https://doi.org/10.1002/anie.202003842.

[57] J. Li, J. Lv, Y.C. Hao, L.W. Chen, Y. Zuo, Y. Liu, S. Li, F. Zhang, F. Deng, A.X. Yin, J. Zhou, P. Li, B. Wang, Nanoporous graphene via a pressing organization calcination strategy for highly efficient electrocatalytic hydrogen peroxide generation, ACS Appl. Mater. Interfaces 13 (2021) 47478–47487, https://doi.org/10.1021/acsami.1c11673.

[58] B.Q. Li, C.X. Zhao, J.N. Liu, Q. Zhang, Electrosynthesis of hydrogen peroxide synergistically catalyzed by atomic Co–N_x–C sites and oxygen functional groups in noble-metal-free electrocatalysts, Adv. Mater. 31 (2019) 1808173, https://doi.org/10.1002/adma.201808173.

[59] F. Wang, J. Xu, Z. Wang, Y. Lou, C. Pan, Y. Zhu, Unprecedentedly efficient mineralization performance of photocatalysis-self-Fenton system towards organic pollutants over oxygen-doped porous g-C_3N_4 nanosheets, Appl. Catal. B Environ. 312 (2022), 121438, https://doi.org/10.1016/j.apcatb.2022.121438.

[60] X. Fu, Y. Han, H. Xu, Z. Su, L. Liu, Electrochemical study of a novel high-efficiency PbO_2 anode based on a cerium-graphene oxide co-doping strategy: Electrodeposition mechanism, parameter optimization, and degradation pathways, J. Hazard. Mater. 422 (2022), 126890, https://doi.org/10.1016/j.jhazmat.2021.126890.

[61] L. Gui, Z. Chen, B. Chen, Y. Song, Q. Yu, W. Zhu, Q. Hu, Y. Liu, Z. Zheng, L. Ze, H. You, F. Yeasmin, Preparation and characterization of ZnO/PEG-Co(II)-PbO_2 nanocomposite electrode and an investigation of the electrocatalytic degradation of phenol, J. Hazard. Mater. 399 (2020), 123018, https://doi.org/10.1016/j.jhazmat.2020.123018.